Domain wall pinning in high temperature SM(Co, Fe, Cu, Zr)$_{7-8}$ magnets

B. Streibl, J. Fidler,[a] and T. Schrefl
Institute of Applied and Technical Physics, Vienna University of Technology, A-1040 Vienna, Austria

A finite element method was used to simulate domain wall pinning in $SmCo_5/Sm_2Co_{17}$ based permanent magnets. The finite element model was built according to the cellular microstructure obtained from transmission electron microscopy investigations. The numerical results show a strong influence of the dimension of the cell boundary phase on the coercive field, which significantly increases with the extension of the 1:5/7-type cell boundary phase. The calculated values of the coercive field are in the range from 1000 to 2000 kA/m assuming a cell size varying from 80 to 160 nm. The difference of the magnetocrystalline anisotropy between cell boundary and cell interior phases is determined by the Cu content of the magnet. © *2000 American Institute of Physics.* [S0021-8979(00)63808-2]

I. INTRODUCTION

Precipitation hardened $SmCo_5/Sm_2Co_{17}$ based permanent magnets have been developed during the past 20 years.[1] It was shown that the influence of the cellular precipitation structure on the coercive field lead to a domain wall pinning controlled mechanism. Recently, new high temperature applications have been developed, and the demand for better soft and hard magnetic materials with sufficient large coercive field and remanence at 400 °C is obvious.[2] The new materials are based on Sm(Co, Fe, Cu, Zr)$_{7.5}$ with a high Cu content and reduced Fe content as compared to conventional SmCo 2:17 type magnets.[3]

With increasing effort to improve the thermal stability of $SmCo_5/Sm_2Co_{17}$ based permanent magnets numerical models have been developed, in order to obtain a better understanding of the pinning mechanism. Katter[4] proposed a two-dimensional model based on the local wall energy to derive the coercivity of Sm(Co, Fe, Cu, Zr)$_{7.5}$ magnets. Chui[5] applied a Monte Carlo method to simulate the pinning of domain walls at finite temperatures.

This work combines microstructural investigations using transmission electron microscopy (TEM) with micromagnetic finite element simulation. The three-dimensional finite element model takes into account the rhombohedral cellular structure of the magnet. According to the transmission electron microscope investigations our micromagnetic simulations assumed a cellular precipitation structure in the range of 50–250 nm. The equilibrium position of the domain walls are calculated from the minimization of the total magnetic Gibb's free energy. Section II describes the TEM investigation of the microstructure. Section III presents the micromagnetic finite element simulations that give a straight forward explanation of the pinning mechanism of Sm(Co, Fe, Cu, Zr)$_{7.5}$ magnets.

II. MICROSTRUCTURE OF "PINNING" CONTROLLED SM(Co, Fe, Cu, Zr)$_{7-8}$ MAGNETS

Cu-containing Co rare-earth magnets with a composition of Sm(Co, Fe, Cu, Zr)$_{7-9}$ exhibit domain wall pinning controlled magnetization curves. TEM studies of such magnets have shown a fine cell morphology with abut 50–200 nm in diameter at the magnetic optimum state.[6,7] The TEM micrograph of Fig. 1 shows the rhombic cells of the type $Sm_2(Co, Fe)_{17}$ (A) which are separated by a Sm(Co, Cu, Zr)$_{5-7}$-cell boundary phase (B). The development of the continuous, cellular precipitation structure of highest coercivity magnets is controlled by the growth process and the chemical redistribution process[8] and is determined by the direction of zero deformation strains due to the lattice misfit between the different phases.[9] The cellular precipitation structure is formed during the isothermal aging procedure, whereas the chemical redistribution of the transition metals during the step aging procedure increases the coercivity of the final magnet. It should be mentioned that the annealing process takes up to 24 h to obtain maximum hard magnetic properties. Growth of the cell structure occurs primarily during the isothermal aging procedure and involves the diffusion of samarium. In magnets with high coercivities (>1000 kA/m) thin platelets (C) are found perpendicular to the hexagonal *c* axis.

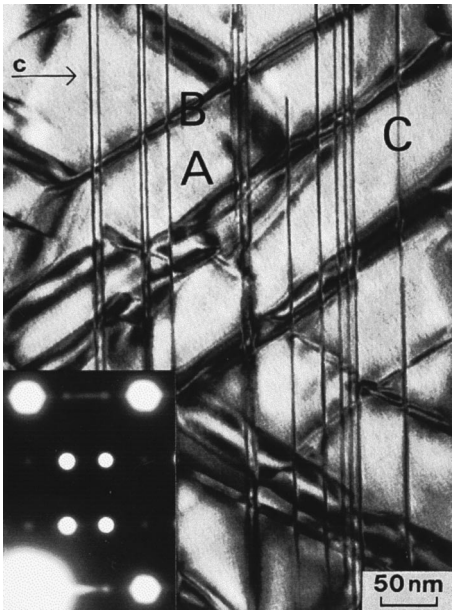

FIG. 1. Transmission electron micrograph and diffraction pattern showing the cellular precipitation structure in a pinning controlled Sm(Co, Fe, Cu, Zr)$_{6-8}$ magnet.

[a]Electronic mail: fidler@mail.tuwien.ac.at

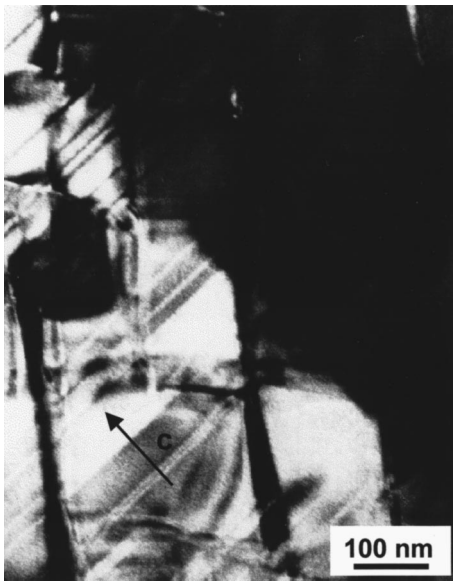

FIG. 2. Foucault image showing the attractive domain wall pinning at the continuous $Sm(Co, Cu, Zr)_{5\text{-}7}$ cell boundary phase.

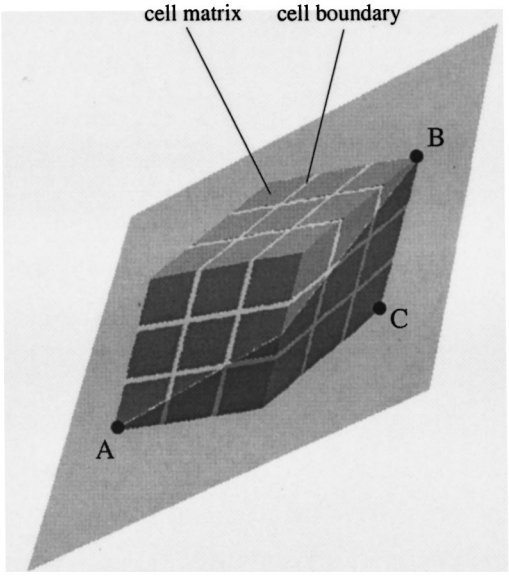

FIG. 3. Three-dimensional model of the microstructure of a the $Sm(Co, Fe, Cu, Zr)_{6\text{-}8}$ magnet used for the finite element simulations. The dark and bright regions denote the rhombohedral cells and the cell boundary phase, respectively. The shaded area denotes a slice plane parallel to the *c* axis for plotting the calculated domain pattern.

High resolution electron microscope investigations show that the crystal structure of the platelet phase is close to the hexagonal Sm_2Co_{17} structure with a *c*-crystal parameter of 0.8 nm, which is in agreement with metallurgical considerations. Contrary to high coercivity magnets which contain large crystallographic twins, a microtwinning within the cell interior phase (A) is observed by high resolution electron microscopy in low coercivity magnets ($<$500 kA/m). In the Lorentz electron microscope Foucault micrograph of Fig. 2 it is shown that the cellular precipitation structure acts as an attractive pinning center for magnetic domain walls. Maximum coercivities (2000 kA/m) were found in magnets with cell diameters of about 200 nm. The compositional difference between the cell boundary phase (B) and the cell interior phase (A) determines the coercive field.[10] The platelet phase (C) predominately acts as a diffusion path for the transition metals and leads to a better chemical redistribution after the isothermal aging treatment and therefore to a higher coercivity of the magnet. Impurities, primarily such as oxygen and carbon, lead to the formation of macroscopic precipitates of the Sm_2O_3,ZrC,TiC, etc., and therefore impede the formation of the platelet phase (C) and finally impede the chemical redistribution process.

III. MICROMAGNETIC SIMULATIONS

The numerical simulation starts from the total magnetic Gibb's free energy E_t which is the sum of the sum of the exchange, the magnetocrystalline anisotropy energy, the magnetostatic energy, and the Zeeman energy of the magnetic polarization in an external field H_{ext}[11]

$$E_t = \int \left[A \sum_{i=1}^{3} (\nabla \beta_i)^2 - K_1 (\mathbf{J}\cdot\mathbf{u})^2 - \frac{1}{2}\mathbf{J}\cdot\mathbf{H}_d - \mathbf{J}\cdot\mathbf{H}_{\text{ext}} \right] dV, \quad (1)$$

where A is the exchange constant, $\mathbf{H}_d$ is the demagnetizing field, K_1 is anisotropy constant, and $\mathbf{u}$ denotes the unit vector parallel to the *c* axis. When the direction cosines of the magnetization β_i are approximated by piecewise linear functions on the finite element mesh, the energy functional (1) reduces to an energy function with the nodal values of the direction cosines as unknowns. Its minimization with respect to the direction cosines of the magnetization at the nodal points variables, subject to the constraint $\beta_1^2+\beta_2^2+\beta_3^2=1$, provides an equilibrium distribution of the magnetization. To satisfy the constraint, the magnetization can be represented by polar coordinates. The resulting algebraic minimization problem is solved using a quasi-Newton conjugate gradient technique.[12] The demagnetizing field $\mathbf{H}_d$ follows from the magnetic scalar potential which is calculated using a hybrid finite element/boundary technique.[13]

Figure 3 shows the rombohedral cellular structure used for the simulations. The model takes into account the cell interior phase (A) and the cell boundary phase (B) but neglects the platelet phase (C). The 27 cells are divided into 90 000 finite elements, using a socalled geometrical mesh.[14] The mesh is gradually refined towards the cell boundary phase, reaching a mesh size comparable to the domain wall width near the cell boundaries. The intrinsic magnetic properties of Ref. 15 are used for the calculations. Durst and co-workers[15] derived the intrinsic magnetic properties of the cell matrix $Sm_2(Co, Fe)_{17}$ and the cell boundary $Sm(Co, Cu, Zr)_{5\text{-}7}$ from the analysis of magnetization curves parallel and perpendicular to the alignment direction. The anisotropy constant of the cell matrix is about 2.6 times larger than the anisotropy constant of the cell boundary phase. The exchange constant was assumed to be the same for both phases, because of similar values of the Curie temperature. The exchange constant was derived from the effective wall energy which was obtained from closure domains of a $Sm(Co, Fe, Cu, Zr)_{7.6}$ magnet. The reduced magnetocrystalline anisotropy of the cell boundary phase lowers the wall energy with the cell boundary and thus gives rise to attrac-

TABLE I. Intrinsic properties of the cell matrix and cell boundary phases used for micromagnetic calculations. The values[15] hold for the compositions $Sm(Co_{0.68}, Fe_{0.22}, Cu_{0.08}, Zr_{0.02})_{6-8}$.

Phase		J_s(T)	K_1(MJ/m^2)	A(pJ/m)
$Sm_2(Co, Fe)_{17}$	Cell matrix	1.19	5	14
$Sm(Co, Cu, Zr)_{5-7}$	Cell boundary	0.8	1.9	14

tive domain wall pinning. Table I summarizes the intrinsic magnetic properties used for the calculations.

The initial state for the calculations was a two domain state with a domain wall just lying in the symmetry plane through points *A*, *B*, and *C* (see Fig. 3). The domain with the magnetization parallel to the field direction grows under the influence of an applied field, which is applied parallel to the *c* axis. The domain wall is pushed towards the cell boundary phase. The wall becomes pinned at the cell boundary, leading to the well known zig-zag domain pattern. Fig. 4 gives the calculated domain patterns in a slice plane parallel to the *c* axis for different applied fields. As the external field is increased the wall breaks away from the cell boundary phase. Depinning of the domain wall starts at the corners of the cell boundary. It should be noted that the domain patterns of Fig. 4 are only a two-dimensional representation of a three-dimensional magnetization structure and are in agreement with the observations in Fig. 2. According to the complex cellular precipitation structure, the domain wall is heavily bent. The depinning causes a further bowing of the domain wall. Furthermore, the thickness of the cell boundary phase is smaller than the domain wall width and therefore a three-dimensional micromagnetic simulation is necessary to derive the pinning field. The high pinning fields obtained in the simulations may be attributed to both the reduced anisotropy of the cell boundary phase and the complex three dimensional geometry of the rombohedral cells.

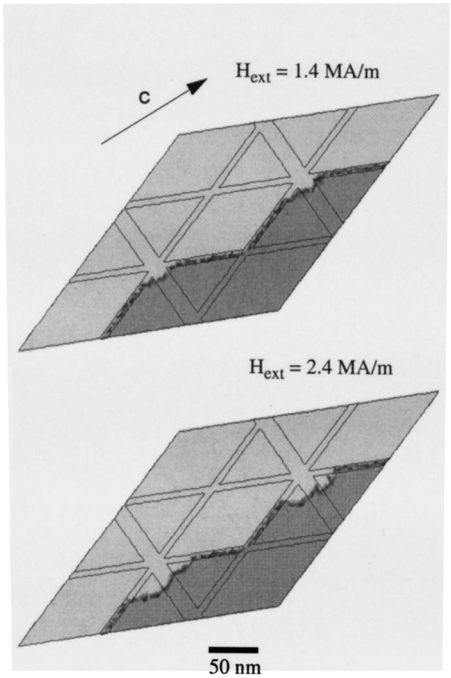

FIG. 4. Calculated domain images at different applied fields for a cell size of 160 nm. The gray scale plot denotes magnetization components parallel to the *c* axis within the slice plane depicted in Fig. 3.

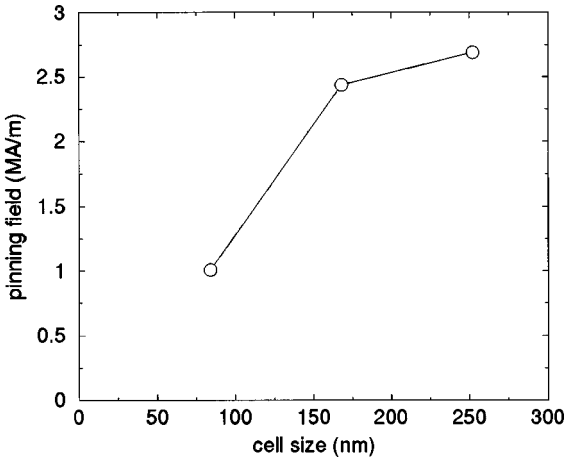

FIG. 5. Calculated pinning field as a function of the cell size.

Figure 5 gives the calculated pinning field as a function of the cell size. Keeping the composition of the magnet constant, the width of the cell boundary increases linearly with increasing cell size. Pinning field in the range of 1–2 MA/m are obtained for a cell size of 80–160 nm. The corresponding values for the thickness of the cell boundaries are 3 and 6 nm.

In order to obtain sufficient high coercivity at high temperatures (>400 °C) the Cu concentration has to be increased.[3] The simulations show that the resulting increase of the difference between the K_1 values of the cell boundary and matrix phases explain the increase of coercivity at high temperatures.

ACKNOWLEDGMENTS

This work was supported by the Austrian Science Fund (Y132-PHY) and the EU project (GRD1-1999-11125).

[1] H. Nagel, J. Appl. Phys. **50**, 1026 (1979).
[2] S. Liu, E. P. Hoffman, and J. R. Brown, IEEE Trans. Magn. **33**, 3859 (1997).
[3] J. F. Liu, Y. Zhang, Y. Ding, D. Dimitrov, and G. C. Hadjipanayis, in *Rare Earth Permanent Magnets for High Temperature Applications* (Werkstoff-Informationsgesellschaft, Dresden, 1998), p. 607–622.
[4] M. Katter, J. Appl. Phys. **83**, 6721 (1998).
[5] S. T. Chui, J. Magn. Magn. Mater. **202**, 133 (1999).
[6] J. Fidler, P. Skalicky, and F. Rothwarf, IEEE Trans. Magn. **MAG-19**, 2041 (1983).
[7] R. K. Mishra, G. Thomas, T. Yoneyama, A. Fukuno, and T. Ojima, J. Appl. Phys. **52**, 2517 (1981).
[8] A. E. Ray, J. Appl. Phys. **55**, 2094 (1984).
[9] J. D. Livingston and D. L. Martin, J. Appl. Phys. **48**, 1350 (1977).
[10] J. Fidler, J. Magn. Magn. Mater. **30**, 58 (1982).
[11] W. F. Brown, Jr., *Micromagnetics* (Wiley, New York, 1963).
[12] P. E. Gill, W. Murray, and M. H. Wright, *Practical Optimization* (Academic, London, 1993).
[13] D. R. Fredkin and T. R. Koehler, IEEE Trans. Magn. **26**, 415 (1990).
[14] B. Szabo and I. Babuska, *Finite Element Analysis* (Wiley, New York, 1991).
[15] K.-D. Durst, H. Kronmüller, and W. Ervens, Phys. Status Solidi A **108**, 403 (1988).